

Research Article

Facile Solvothermal Synthesis of BiOCl/ZnO Heterostructures with Enhanced Photocatalytic Activity

Yong-Fang Li,¹ Ming Zhang,² Dan-Lu Guo,³ Fei-Xia He,³ Ying-Zhu Li,³ and Ai-Jun Wang³

¹College of Chemistry and Chemical Engineering, Henan Institute of Science and Technology, Xinxiang 453003, China

²School of Chemistry and Chemical Engineering, Henan Normal University, Xinxiang 453007, China

³College of Geography and Environmental Science, Zhejiang Normal University, Jinhua 321000, China

Correspondence should be addressed to Ai-Jun Wang; ajwang@zjnu.cn

Received 3 October 2014; Accepted 7 December 2014; Published 18 December 2014

Academic Editor: Gong-Ru Lin

Copyright © 2014 Yong-Fang Li et al. This is an open access article distributed under the Creative Commons Attribution License, which permits unrestricted use, distribution, and reproduction in any medium, provided the original work is properly cited.

Well-defined nanosheet-assembled $(\text{BiOCl})_x(\text{ZnO})_{1-x}$ nanoflowers were synthesized by a solvothermal method. It was found that ZnO nanoparticles were anchored on the flower-like BiOCl nanostructures, as demonstrated by varying the initial compositions of the Bi precursor and the volume ratios of mixed solvents (ethylene glycol to water). The as-prepared $(\text{BiOCl})_{0.6}(\text{ZnO})_{0.4}$ nanocomposites showed enhanced photocatalytic activity toward rhodamine B degradation under ultraviolet (UV) irradiation. And the photocatalytic mechanism was discussed in detail.

1. Introduction

Zinc oxide (ZnO) has broad applications in transparent electronics, solar cells, piezoelectric devices, chemical sensors, spin electronics, and optical devices, owing to its excellent electrical, biocompatible, optical, and chemical properties [1–6]. However, only ultraviolet light ($\lambda < 385$ nm) can be utilized for pure ZnO, because of its wide band gap energy (3.37 eV) that severely hinders its practical applications [1, 2, 7, 8]. Furthermore, the fast recombination rate of photogenerated electron-hole pairs is another critical drawback in photocatalytic reactions. Therefore, it is still a challenge to extend its photoresponses and improve the separation efficiency of electron-hole pairs.

To date, one effective approach is to modify ZnO surface with a narrow and proper band gap semiconductor, because the built-in potential gradient at the interface promotes the separation of electron-hole pairs and reduces the chance of recombination, resulting in the improved photocatalytic efficiency as compared to pure ZnO counterparts [9, 10]. Therefore, a series of hybrid nanomaterials were prepared, on the basis of ZnO coupled with many metals (e.g., Ce, Al, Cr, Ag, and Zr) [11–14], metal oxides (e.g., TiO_2 , SnO_2 , and Bi_2O_3) [15–18], and metal sulfides (e.g., Cu_2S and CdS) [19–21].

Recently, bismuth oxyhalides (BiOX , $X = \text{Cl}$, Br , and I) display unique optical properties such as the improved photocatalytic activity on the degradation of organic contaminant [15] and industrial applications [22–24], compared with single counterparts. Zhang and coworkers synthesized BiOI/TiO_2 heterostructures at low temperature [15]. Lately, BiOCl with heterostructures as a kind of new photocatalyst has attracted great attention [25–28]. For example, Cheng's groups prepared Bi_2S_3 nanocrystals/ BiOCl nanocomposites under solvothermal conditions [25]. Weng et al. constructed Bi/ BiOCl hybrid nanosheets by a UV light-induced chemical reduction route [26].

In this work, a facile solvothermal method was developed to prepare monodisperse nanosheet-assembled nanoflowers of $(\text{BiOCl})_x(\text{ZnO})_{1-x}$. Their photocatalytic activity was investigated through the degradation of rhodamine B (RhB) under ultraviolet (UV) irradiation. And the possible photocatalytic mechanism was discussed in some detail.

2. Experimental Section

2.1. Chemicals and Materials. Ethylene glycol (EG), $\text{Zn}(\text{Ac})_2 \cdot 2\text{H}_2\text{O}$, $\text{Bi}(\text{NO}_3)_3 \cdot 5\text{H}_2\text{O}$, and rhodamine B were purchased from Shanghai Chemical Reagent Corporation. All the other chemicals were of analytical grade and used as received.

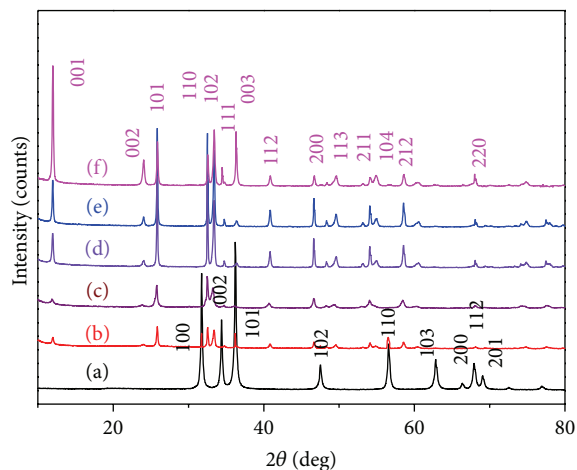


FIGURE 1: XRD patterns of the $(\text{BiOCl})_x(\text{ZnO})_{1-x}$ powders: ZnO (curve (a)), $(\text{BiOCl})_{0.4}(\text{ZnO})_{0.6}$ (curve (b)), $(\text{BiOCl})_{0.6}(\text{ZnO})_{0.4}$ (curve (c)), $(\text{BiOCl})_{0.7}(\text{ZnO})_{0.3}$ (curve (d)), $(\text{BiOCl})_{0.75}(\text{ZnO})_{0.25}$ (curve (e)), and BiOCl (curve (f)).

All the aqueous solutions were prepared with twice-distilled water throughout the whole experiments.

2.2. Preparation. For preparation of $(\text{BiOCl})_x(\text{ZnO})_{1-x}$ heterostructures, different amounts of $\text{Bi}(\text{NO}_3)_3 \cdot 5\text{H}_2\text{O}$ were slowly put into 15 mL of EG solution containing 0.01 mol of $\text{Zn}(\text{Ac})_2$ under stirring for 1 h, followed by dropwise addition of 5 mL of water. Next, 5 mL of KCl solution with the same content of $\text{Bi}(\text{NO}_3)_3$ was put into the mixed solution and continuously stirred for 1 h. The resulting mixture was transferred into 50 mL Teflon-lined stainless steel autoclave, sealed tightly, heated at 120°C for 12 h, and then cooled to room temperature naturally. Finally, the products were collected by thoroughly washing with water and ethanol and dried in vacuum at 50°C . The BiOCl contents (wt%) were 0%, 40%, 60%, 70%, 75%, and 100%, denoted by ZnO, $(\text{BiOCl})_{0.4}(\text{ZnO})_{0.6}$, $(\text{BiOCl})_{0.6}(\text{ZnO})_{0.4}$, $(\text{BiOCl})_{0.7}(\text{ZnO})_{0.3}$, $(\text{BiOCl})_{0.75}(\text{ZnO})_{0.25}$, and BiOCl of the final products, respectively.

For comparison, pure BiOCl and ZnO were mechanically mixed (denoted by $(\text{BiOCl})_x + (\text{ZnO})_{1-x}$) to evaluate the role of heterojunctions on the photocatalytic activity of the BiOCl/ZnO samples.

2.3. Characterization. The crystal structures of the samples were characterized by X-ray diffraction (XRD) on a Bruker-D8-AXS diffractometer system equipped with a $\text{Cu K}\alpha$ source. The morphology and particle size were analyzed by a scanning electron microscope (SEM, JEOL-JSM-6390 LV). Transmission electron microscopy (TEM) and high-resolution TEM (HRTEM) images were obtained with a JEOL JEM-2100F system at 200 kV accelerating voltage. A small amount of the sample was prepared by dispersing the final products in ethanol by ultrasonication and then a drop of the solution was deposited on a Cu grid for TEM observation. UV-vis diffuse reflectance spectra (DRS) were analyzed by

a PerkinElmer Lambda 950 UV-vis spectrometer and BaSO_4 was used as a reference. X-ray photoelectron spectra (XPS) were recorded by using a K-Alpha ($\text{K}\alpha$) XPS spectrometer (ThermoFisher, E. Grinstead, UK) with an Al $\text{K}\alpha$ X-ray radiation (1486.6 eV) for excitation. The contaminant carbon ($\text{C}_{1s} = 284.6$ eV) was used as a standard to calibrate all binding energies.

2.4. Photocatalytic Measurements. The photocatalytic ability of the samples was examined by photocatalytic decolorization of RhB in aqueous solution using UV irradiation at ambient temperature. A 300 W Hg lamp (Yaming Company, Shanghai, 8 cm away from the suspension) was used as a light source to trigger the photocatalytic reaction. Typically, 0.06 g of the sample was put into a 60 mL of the RhB solution (40 mg L^{-1}) in a reaction cell with a Pyrex jacket. Before irradiation with UV, the suspension was stirred for 1 h in dark to reach an adsorption-desorption equilibrium. After irradiation for different time intervals, the samples were taken out from the reaction system, centrifuged at 12000 rpm for 10 min to remove the photocatalyst, followed by measuring the corresponding UV-vis spectra. All the experiments were conducted at room temperature.

3. Results and Discussion

3.1. Characterization of the BiOCl/ZnO Heterostructures. Solvothermal synthesis is a robust method for preparing heterostructures such as alloys and homogeneous compositions that display practical applications in catalytic field and thereby is an advantageous way to tune the properties of a catalyst [4]. X-ray diffraction (XRD) patterns of the $(\text{BiOCl})_x(\text{ZnO})_{1-x}$ heterostructures (Figure 1) exhibit typical diffraction peaks corresponding to the wurtzite structured ZnO (JCPDS card number 36-1451) and/or the tetragonal phase BiOCl (JCPDS card number 06-0249), respectively. The sharp peaks reveal a high degree of crystallization for the products. Furthermore, with the increase of the BiOCl content (wt%) up to 100%, the peaks from BiOCl are gradually increased, while the peaks from ZnO phase are almost unchanged as the BiOCl content (wt%) is at or above 60% (Figure 1, curve c–f). It means crystal growth inhibition of ZnO for the existence of BiOCl. Additionally, no other crystalline impurities are detected, further confirming high purity of the products.

The surface chemical compositions and oxidation states of the $(\text{BiOCl})_x(\text{ZnO})_{1-x}$ heterostructures were further investigated by X-ray photoelectron spectroscopy (XPS). Taking the surface of the $(\text{BiOCl})_{0.6}(\text{ZnO})_{0.4}$ sample as an example (see Figure S1 in Supplementary Material available online at <http://dx.doi.org/10.1155/2014/347061>), Zn, O, Bi, Cl, and a trace amount of C elements coexist based on the XPS survey spectrum. Moreover, as revealed by high-resolution XPS spectra (Figure 2), the peaks located at 1021.5 and 1044.7 eV are assigned to the binding energy of $\text{Zn}_{2p_{3/2}}$ and $\text{Zn}_{2p_{1/2}}$, respectively (Figure 2(a)), which are in good agreement with those in ZnO structures [7]. The peaks emerged at 159.0 and 164.3 eV are attributed to the binding energy of $\text{Bi}_{4f_{7/2}}$ and $\text{Bi}_{4f_{5/2}}$, respectively (Figure 2(b)), which

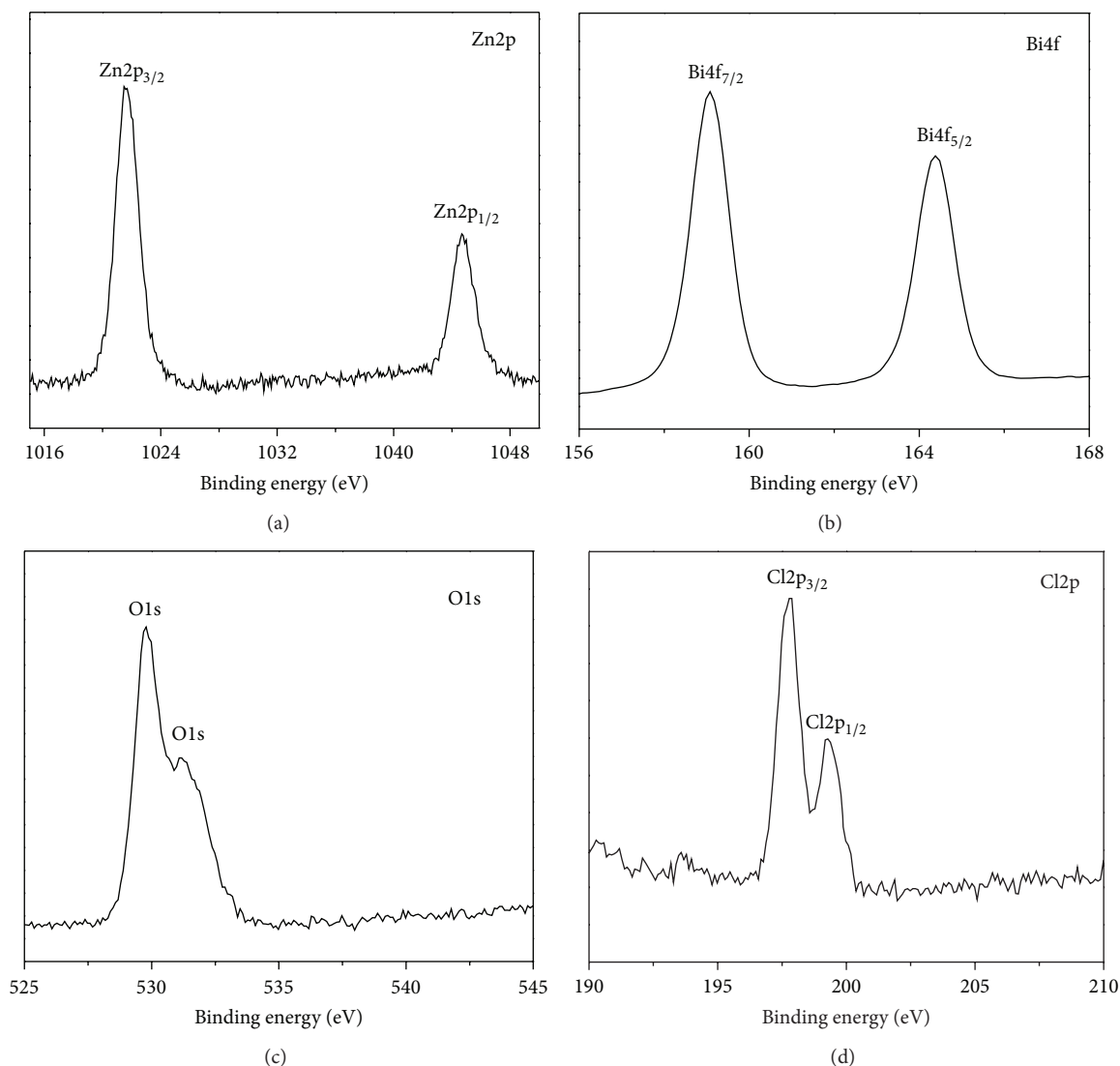


FIGURE 2: High-resolution XPS spectra of the $(\text{BiOCl})_{0.6}(\text{ZnO})_{0.4}$ powders: Zn_{2p} (a), Bi_{4f} (b), O_{1s} (c), and Cl_{2p} (d).

are associated with Bi^{3+} and Bi^{4+} [15, 29], respectively. Meanwhile, the satellite peaks appeared near the peaks of $\text{Bi}_{4f7/2}$ and $\text{Bi}_{4f5/2}$ with a distance of 1.8 eV, which is similar to that in the previous literature [15]. And an asymmetric peak of O_{1s} is detected (Figure 2(c)), indicating the presence of two oxygen species in the adjacent regions. The peak at 531.1 eV corresponds to the Zn–O bonds [7], whereas the peak at 529.1 eV is attributed to the Bi–O bond in Bi_2O_3 slabs of BiOCl layered structures [15]. In addition, the peaks at 197.7 ($\text{Cl}_{2p3/2}$) and 199.2 ($\text{Cl}_{2p1/2}$) eV are ascribed to pure BiOCl in the XPS spectrum of the Cl_{2p} core level (Figure 2(d)). The above XRD and XPS analysis confirm the coexistence of BiOCl and ZnO in the $(\text{BiOCl})_x(\text{ZnO})_{1-x}$ heterostructures, while either Bi or Cl species is not incorporated into ZnO lattice because of low temperature, as supported by the XRD data.

The physicochemical property of one solvent is essential to its solubility, reactivity, and diffusion behaviors, along

with its intermediates [30]. In this system, the growth of $(\text{BiOCl})_{0.6}(\text{ZnO})_{0.4}$ heterostructures strongly depends on the mixed solvents of EG and water by varying their volume ratios (Figure 3), while other conditions are kept the same. Using EG as a single solvent yields numerous interconnected nanosheet-assembled spheres with the average diameter of 2 μm (Figure 3(a)). When the volume ratio of EG to water is 23:2 (Figure 3(b)), similar spheres are obtained, while their size is enlarged to 10 μm . These microspheres are assembled by a lot of nanoplates aligned radially and tightly with several nanometers in thickness, as revealed by higher magnification SEM image (inset in Figure 3(b)). Interestingly, by reducing the ratio to 21:4, some microspheres are transformed to sheet-like nanostructures (Figure 3(c)). Flower-like structures are dominated with the ratio of 18:7 (Figure 3(d)), in which each flower contains four petals assembled by nanosheets. Decreasing the ratio to 15:10 produces many well-defined microflowers with smaller diameter of 4–5 μm

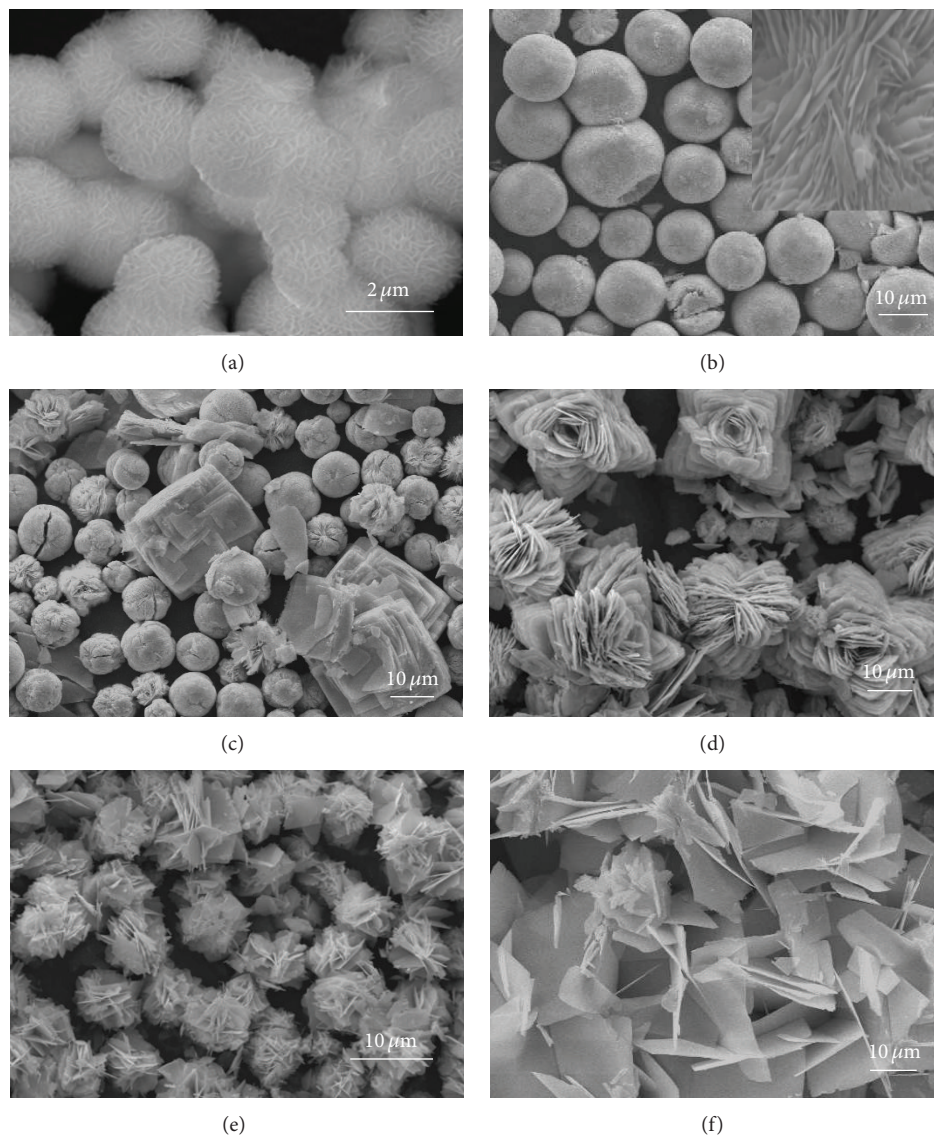


FIGURE 3: SEM images of the $(\text{BiOCl})_{0.6}(\text{ZnO})_{0.4}$ composites prepared by different volume ratios of EG to water: (a) 25 : 0, (b) 23 : 2, (c) 21 : 4, (d) 18 : 7, (e) 15 : 10, and (f) 0 : 25.

(Figure 3(e)). However, a large number of nanoplates are obtained only using water as a solvent (Figure 3(f)).

In our work, water is an amphiprotic solvent, where most inorganic salts are readily dissolved. In contrast, EG possesses strong chelation, which can coordinate with free Bi^{3+} and Zn^{2+} to form alkoxides, leading to the decrease of the growth rate of BiOCl and ZnO . This is ascribed to the fact that EG molecules can exist in long chains where hydrogen bonds are formed between hydroxyl groups [23]. Herein, EG acts as a soft template and directs the growth of heterogeneous nanoparticles into nanoplates at the very early stage, followed by the EG-induced self-assembly of unstable microspheres, eventually resulting in well-defined microspheres via a dissolution-recrystallization process, as demonstrated by the SEM experiments (Figure 3).

Furthermore, the amount of the Bi precursor is also important for the $(\text{BiOCl})_x(\text{ZnO})_{1-x}$ heterostructures

(Figure 4), while other conditions remain constant. The absence of the Bi precursor yields plenty of ZnO flowers assembled by many smooth nanoplates, with the average diameter of 3–6 μm (Figure S2A, Supporting Information). In the presence of 40% BiOCl , the products contain a series of flower-like spheres with the mean diameter size of 4 μm , which are built by many nanopetals connected together from the centre to form flower-like structures (Figure 4(a)). Similar structures are obtained by increasing the supply of BiOCl up to 75% (Figures 4(c)–4(d)). However, the only presence of the Bi precursor produces uniform apple-like BiOCl hierarchical structures with the average diameter of 3 μm (Figure S2B, Supporting Information). These results indicate that the Bi precursor is critical to the formation of the $(\text{BiOCl})_x(\text{ZnO})_{1-x}$ nanocomposites.

A more detailed insight of the $(\text{BiOCl})_{0.6}(\text{ZnO})_{0.4}$ heterostructures was examined by TEM and HRTEM

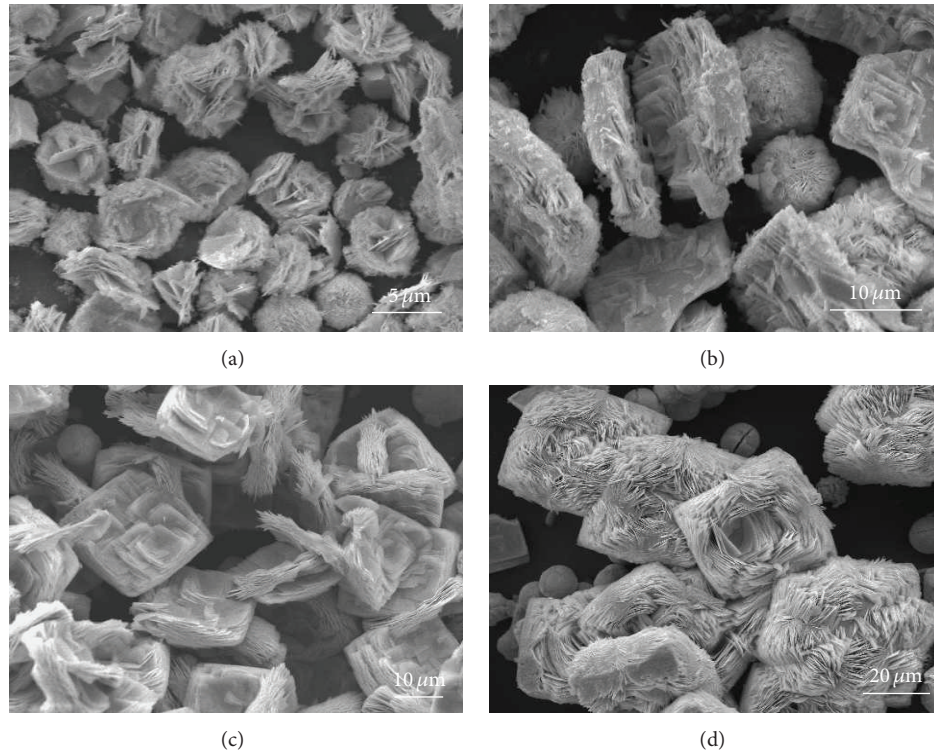


FIGURE 4: SEM images of the $(\text{BiOCl})_x(\text{ZnO})_{1-x}$ composites: $(\text{BiOCl})_{0.4}(\text{ZnO})_{0.6}$ (a), $(\text{BiOCl})_{0.6}(\text{ZnO})_{0.4}$ (b), $(\text{BiOCl})_{0.7}(\text{ZnO})_{0.3}$ (c), and $(\text{BiOCl})_{0.75}(\text{ZnO})_{0.25}$ (d).

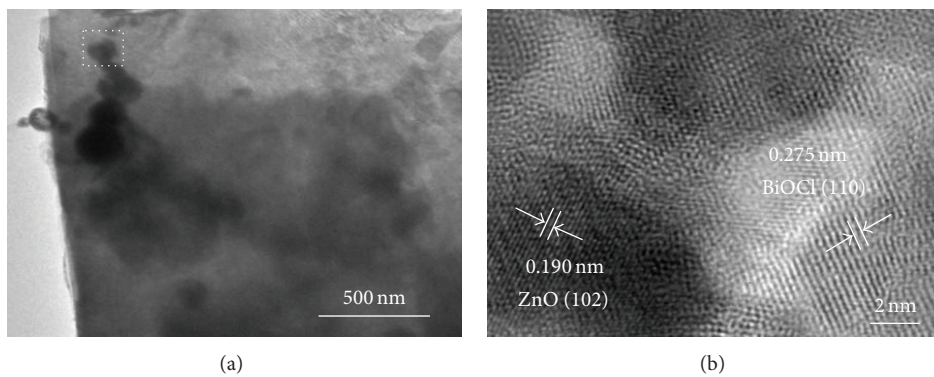


FIGURE 5: TEM (a) and HRTEM (b) images of the $(\text{BiOCl})_{0.6}(\text{ZnO})_{0.4}$ composites.

measurements after dispersion of the sample under ultrasonication (Figure 5). Some nanoparticles are still attached but not peeled off from the sheet-like subunits (Figure 5(a)), indicating the strong interactions between the ZnO nanoparticles and the sheets. The as-prepared composites are highly crystallized, as confirmed by the lattice fringes with a d -spacing values of 0.275 nm and 0.190 nm from the HRTEM measurements (Figure 5(b)), corresponding to the (110) planes of BiOCl [26–28] and the (102) planes of ZnO [31, 32], respectively, indicating the coexistence of BiOCl and ZnO in the present synthesis. The ZnO nanoparticles exist in the nanosheets subunits of the BiOCl flowers. Meanwhile, the ZnO nanoparticles further confirm why the associated ZnO diffraction peaks are difficult to distinguish when the content of BiOCl is at or above 60%.

3.2. Optical Properties. The UV-vis diffuse reflectance spectra (DRS) patterns of the $(\text{BiOCl})_x(\text{ZnO})_{1-x}$ composites reveal the optical responses are greatly changed in the range of 350–420 nm (Figure 6(a)). Varying the BiOCl content has significant effects on the absorption peak for the samples. This is ascribed to light absorption of BiOCl nanoparticles on the ZnO nanosheet. The band gap energy (E_g) of a semiconductor would be estimated from the following equation:

$$\alpha h\nu = A (h\nu - E_g)^{n/2}, \quad (1)$$

where α , ν , E_g , and A are absorption coefficient, light frequency, band gap energy, and a constant, respectively. For individual ZnO or BiOCl, the value of n is 4 for the indirect transition. As displayed in Figure 6(b), the E_g for

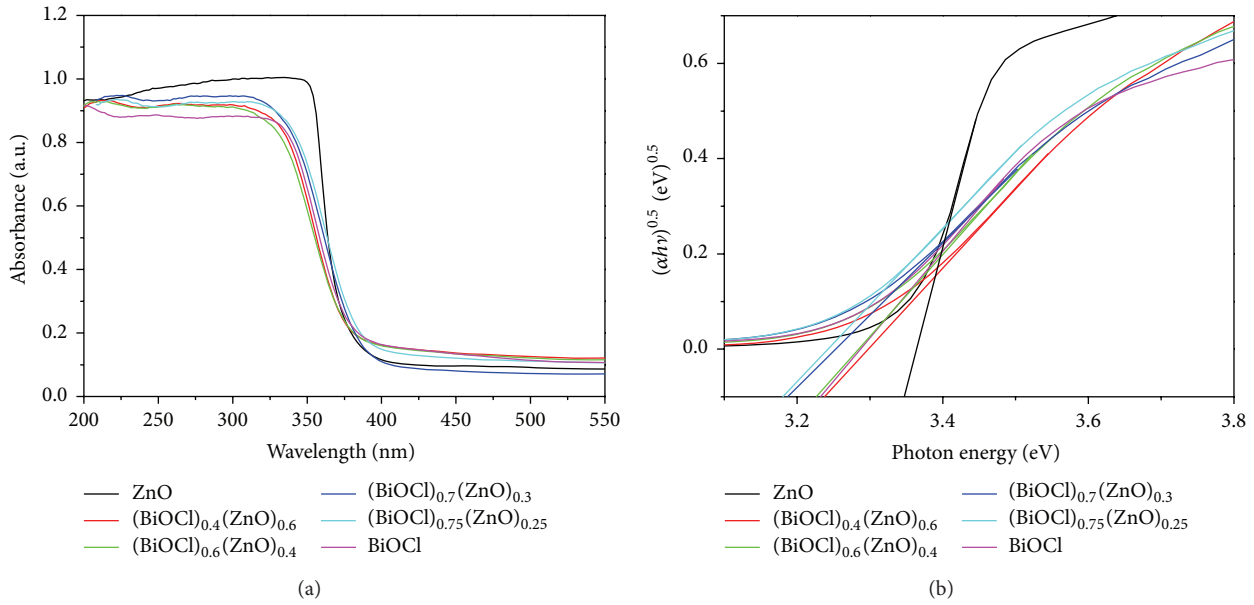


FIGURE 6: (a) UV-vis diffuse reflectance spectra of the $(\text{BiOCl})_x(\text{ZnO})_{1-x}$ composites. (b) The corresponding plot of $(\alpha h\nu)^{0.5}$ versus photon energy.

TABLE 1: Band gaps and photocatalytic activities of the $(\text{BiOCl})_x(\text{ZnO})_{1-x}$ composites.

Samples	Band gap (eV)	k (min^{-1})
ZnO	3.35	0.00030
$(\text{BiOCl})_{0.4}(\text{ZnO})_{0.6}$	3.24	0.00539
$(\text{BiOCl})_{0.6}(\text{ZnO})_{0.4}$	3.22	0.00732
$(\text{BiOCl})_{0.7}(\text{ZnO})_{0.3}$	3.19	0.00465
$(\text{BiOCl})_{0.75}(\text{ZnO})_{0.25}$	3.18	0.00241
BiOCl	3.23	0.00014
$(\text{BiOCl})_{0.6} + (\text{ZnO})_{0.4}$	—	0.00214

the $(\text{BiOCl})_x(\text{ZnO})_{1-x}$ composites can be determined by the intercept of the tangent to the x -axis (Table 1), which is slightly decreased as the content of BiOCl is increased, accompanied with the slight red shift of the associated absorption peaks (Figure 6(a)), owing to the recombination of BiOCl and ZnO in this work.

3.3. Photocatalytic Activity. It is known that the absorption in UV region would increase the number of photogenerated electrons and holes in the photocatalytic reaction [20]. RhB is a kind of chemically stable dye pollutants. Herein, the photolysis of RhB by UV irradiation is significant under our experimental conditions. Thus, the photocatalytic ability of the $(\text{BiOCl})_x(\text{ZnO})_{1-x}$ composites was investigated, using the photocatalytic degradation of RhB by UV irradiation as a model system. Taking the $(\text{BiOCl})_{0.6}(\text{ZnO})_{0.4}$ composites as an example, a series of UV-vis absorption spectra were recorded in a 60 mL aqueous solution containing 40 mg L^{-1} RhB and $0.06 \text{ g } (\text{BiOCl})_{0.6}(\text{ZnO})_{0.4}$ at different time intervals (Figure 7, curves (a)–(i)). The characteristic absorption peak

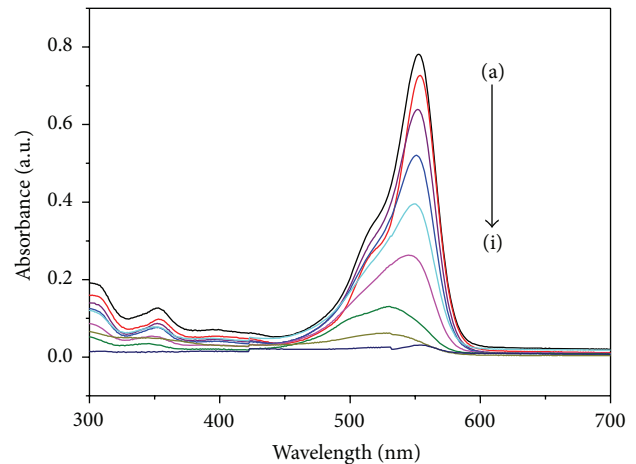


FIGURE 7: UV-vis absorption spectra of the RhB solution (40 mg L^{-1}) containing 1.0 mg mL^{-1} $(\text{BiOCl})_{0.6}(\text{ZnO})_{0.4}$ composites at different time intervals; (a) to (i) 0 min, 10 min, 20 min, 40 min, 60 min, 80 min, 100 min, 120 min, and 140 min.

of RhB at 551 nm quickly decreases by increasing the irradiation time and even disappears when the time is 140 min, indicating complete degradation of RhB in the system.

During the photocatalytic reaction process, using the mechanically mixed $(\text{BiOCl})_{0.6} + (\text{ZnO})_{0.4}$ instead of the $(\text{BiOCl})_{0.6}(\text{ZnO})_{0.4}$ composites, while other conditions remain constant (Figure 8), the absorption peak of RhB at 551 nm is slightly decreased, implying the existence of heterojunctions between BiOCl and ZnO in the $(\text{BiOCl})_{0.6}(\text{ZnO})_{0.4}$ composites. This is due to the effective separation of electron-hole pairs from ZnO by the heterojunctions and the abundant hydroxyl groups

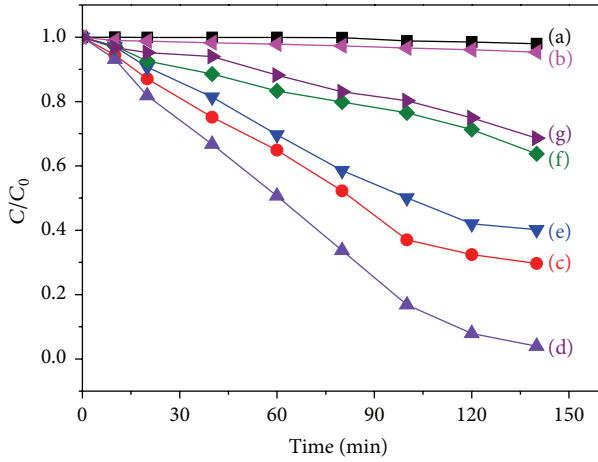


FIGURE 8: Photocatalytic activities of the $(\text{BiOCl})_x(\text{ZnO})_{1-x}$ composites ((a) to (f) ZnO, BiOCl, $(\text{BiOCl})_{0.4}(\text{ZnO})_{0.6}$, $(\text{BiOCl})_{0.6}(\text{ZnO})_{0.4}$, $(\text{BiOCl})_{0.7}(\text{ZnO})_{0.3}$, and $(\text{BiOCl})_{0.75}(\text{ZnO})_{0.25}$) and the mixture of $(\text{BiOCl})_{0.6} + (\text{ZnO})_{0.4}$ (g) on the degradation of RhB under UV irradiation.

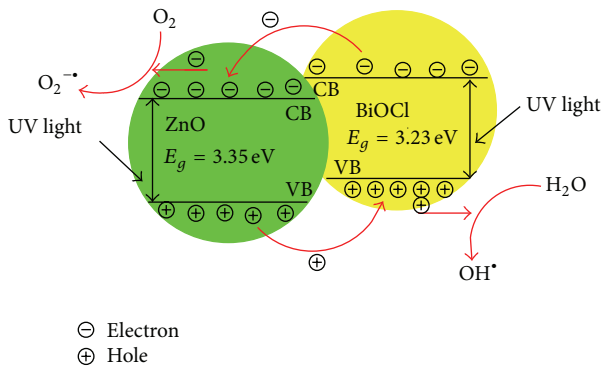


FIGURE 9: Schematic illustration of the electron-transfer process in the $(\text{BiOCl})_x(\text{ZnO})_{1-x}$ heterostructures under UV irradiation.

on the samples surface. However, further increasing the content of BiOCl (e.g., the $(\text{BiOCl})_{0.4}(\text{ZnO})_{0.6}$ and $(\text{BiOCl})_{0.7}(\text{ZnO})_{0.3}$ samples) leads to incomplete degradation of RhB, because excess BiOCl would cover the surface active sites of ZnO. Interestingly, single ZnO and BiOCl in the reaction media would cause negligible RhB degradation with the value of 4% and 6%, respectively. It indicates that the coupling of BiOCl with ZnO clearly contributed to the degradation of RhB. These results demonstrate the enhanced photocatalytic activity of the $(\text{BiOCl})_{0.6}(\text{ZnO})_{0.4}$ composites among the $(\text{BiOCl})_x(\text{ZnO})_{1-x}$ composites.

In addition, the stability of the $(\text{BiOCl})_{0.6}(\text{ZnO})_{0.4}$ composites was examined. After repeated use of the catalysts for 5 times, the degradation of RhB still remained above 85% of their initial values ($\sim 96\%$). Meanwhile, for a storage period of 2 months, the RhB degradation is above 90% of their initial values under the same conditions. These results mean that the $(\text{BiOCl})_{0.6}(\text{ZnO})_{0.4}$ composites can be recycled and stored.

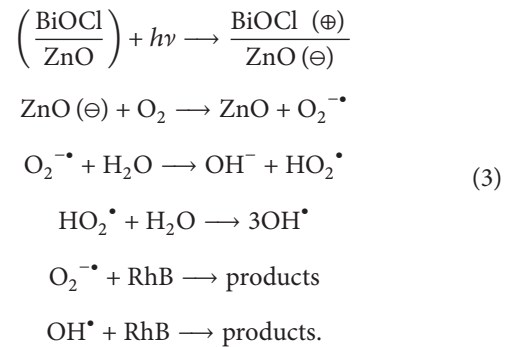
Assuming initial low concentration of the pollutant, the pseudo-first-order model was used to elucidate the reaction kinetics, as expressed by

$$\ln\left(\frac{C_0}{C}\right) = kt, \quad (2)$$

where C/C_0 was used to denote the percentage of degradation, C is the concentration of RhB after degradation and C_0 is the initial concentration of RhB, and k is the pseudo-first-order rate constant. The rate constant for the $(\text{BiOCl})_x(\text{ZnO})_{1-x}$ composites was calculated from Figure 8 and listed in Table 1. When the BiOCl content is at or below 60%, the rate constant (k) increases, and the band gap is reduced. The k achieves the maximum by increasing the BiOCl content to 75% and then reversely decreases, albeit with the decreased band gap. It is known that the k represents the photocatalytic degradation activity. Therefore, with the increase of the k , the photocatalytic degradation activity is increased. These results demonstrate that the $(\text{BiOCl})_{0.6}(\text{ZnO})_{0.4}$ composites are much more effective, compared with the other cases.

When the $(\text{BiOCl})_x(\text{ZnO})_{1-x}$ composites are irradiated by UV light, the excited electrons in the conduction band (CB) of BiOCl easily jump into the CB of ZnO, because of their different band energy. Meanwhile, the holes that emerged in the valence band (VB) of ZnO can migrate to that of BiOCl, which can react with the adsorbed water on the surface of the BiOCl nanoparticles to form highly reactive hydroxyl radicals (OH^\bullet). These hydroxyl radicals can oxidize and destroy organic molecules. Meanwhile, the CB electrons accumulated on the ZnO surface are removed by dissolved O_2 molecules to form highly oxidative species such as OH^\bullet and superoxide radical ($\text{O}_2^{\bullet-}$), which can degrade organic molecules effectively.

Specifically, the photocatalytic degradation of RhB is initiated through the formation of electron-hole pairs on the surface of the photocatalyst (Figure 9). The possible mechanism might be described as follows:



In general, the enhanced photocatalytic activity of BiOCl/ZnO heterostructures is attributed to the synergistic photocatalytic effects between BiOCl and ZnO, its strong absorption in the UV region, and low recombination rate of the electron-hole pairs because of the heterojunction formed between BiOCl and ZnO. Therefore, the prepared composites can be explored as a promising photocatalyst for the degradation of organic pollutants in dyeing and printing industry.

4. Conclusions

In summary, well-defined nanosheet-assembled nanoflowers of $(\text{BiOCl})_x(\text{ZnO})_{1-x}$ with various compositions were synthesized by a simple solvothermal method. The initial content of the Bi precursor and the mixed solvent with different volume ratios of EG to water are essential for the final size, morphology, and composition of the product. The $(\text{BiOCl})_{0.6}(\text{ZnO})_{0.4}$ composites exhibit improved photocatalytic activity toward the degradation of RhB under UV irradiation. The improved photocatalytic activity is attributed to the unique $(\text{BiOCl})_{0.6}(\text{ZnO})_{0.4}$ heterostructures and the synergistic effects between BiOCl and ZnO, which promote the photoelectrons transfer and thereby inhibit their recombination with holes. The developed strategy about surface structure-property correlation can be further generalized and applied for the design of advanced functional nanomaterials and degradation of organic pollutants in dyeing and printing industry.

Conflict of Interests

The authors declare that there is no conflict of interests regarding the publication of this paper.

Acknowledgment

This work was financially supported by the National Natural Science Foundation (no. 21275130).

References

- [1] Q. Xie, J. Li, Q. Tian, and R. Shi, "Template-free synthesis of zinc citrate yolk-shell microspheres and their transformation to ZnO yolk-shell nanospheres," *Journal of Materials Chemistry*, vol. 22, no. 27, pp. 13541–13547, 2012.
- [2] A.-J. Wang, Q.-C. Liao, J.-J. Feng, P.-P. Zhang, A.-Q. Li, and J.-J. Wang, "Apple pectin-mediated green synthesis of hollow double-caged peanut-like ZnO hierarchical superstructures and photocatalytic applications," *CrystEngComm*, vol. 14, no. 1, pp. 256–263, 2012.
- [3] Y.-M. Sung, K. Noh, W.-C. Kwak, and T. G. Kim, "Enhanced glucose detection using enzyme-immobilized ZnO/ZnS core/sheath nanowires," *Sensors and Actuators B: Chemical*, vol. 161, no. 1, pp. 453–459, 2012.
- [4] J.-J. Feng, Q.-C. Liao, A.-J. Wang, and J.-R. Chen, "Mannite supported hydrothermal synthesis of hollow flower-like ZnO structures for photocatalytic applications," *CrystEngComm*, vol. 13, no. 12, pp. 4202–4210, 2011.
- [5] P. Zhu, J. Zhang, Z. Wu, and Z. Zhang, "Microwave-assisted synthesis of various ZnO hierarchical nanostructures: effects of heating parameters of microwave oven," *Crystal Growth and Design*, vol. 8, no. 9, pp. 3148–3153, 2008.
- [6] J.-J. Feng, Z.-Z. Wang, Y.-F. Li, J.-R. Chen, and A.-J. Wang, "Control growth of single crystalline ZnO nanorod arrays and nanoflowers with enhanced photocatalytic activity," *Journal of Nanoparticle Research*, vol. 15, pp. 1565–1577, 2013.
- [7] L. Ge, X. Jing, J. Wang et al., "Trisodium citrate assisted synthesis of ZnO hollow spheres via a facile precipitation route and their application as gas sensor," *Journal of Materials Chemistry*, vol. 21, no. 29, pp. 10750–10754, 2011.
- [8] K.-M. Fang, Z.-Z. Wang, M. Zhang, A.-J. Wang, Z.-Y. Meng, and J.-J. Feng, "Gelatin-assisted hydrothermal synthesis of single crystalline zinc oxide nanostars and their photocatalytic properties," *Journal of Colloid and Interface Science*, vol. 402, pp. 68–74, 2013.
- [9] J. R. Bolton, S. J. Strickler, and J. S. Connolly, "Limiting and realizable efficiencies of solar photolysis of water," *Nature*, vol. 316, no. 6028, pp. 495–500, 1985.
- [10] O. Khaselev and J. A. Turner, "A monolithic photovoltaic-photoelectrochemical device for hydrogen production via water splitting," *Science*, vol. 280, no. 5362, pp. 425–427, 1998.
- [11] N. C. S. Selvam, J. J. Vijaya, and L. J. Kennedy, "Effects of morphology and Zr doping on structural, optical, and photocatalytic properties of ZnO nanostructures," *Industrial & Engineering Chemistry Research*, vol. 51, no. 50, pp. 16333–16345, 2012.
- [12] H. R. Liu, G. X. Shao, J. F. Zhao et al., "Worm-like Ag/ZnO core-shell heterostructural composites: fabrication, characterization, and photocatalysis," *Journal of Physical Chemistry C*, vol. 116, no. 30, pp. 16182–16190, 2012.
- [13] B. Subash, B. Krishnakumar, M. Swaminathan, and M. Shanthi, "Highly efficient, solar active, and reusable photocatalyst: Zr-loaded Ag-ZnO for reactive red 120 dye degradation with synergistic effect and dye-sensitized mechanism," *Langmuir*, vol. 29, no. 3, pp. 939–949, 2013.
- [14] D. Lin, H. Wu, R. Zhang, and W. Pan, "Enhanced photocatalysis of electrospun Ag-ZnO heterostructured nanofibers," *Chemistry of Materials*, vol. 21, no. 15, pp. 3479–3484, 2009.
- [15] X. Zhang, L. Zhang, T. Xie, and D. Wang, "Low-temperature synthesis and high visible-light-induced photocatalytic activity of BiOI/TiO₂ heterostructures," *Journal of Physical Chemistry C*, vol. 113, no. 17, pp. 7371–7378, 2009.
- [16] F.-X. Xiao, "Construction of highly ordered ZnO-TiO₂ nanotube arrays (ZnO/TNTs) heterostructure for photocatalytic application," *ACS Applied Materials & Interfaces*, vol. 4, no. 12, pp. 7055–7063, 2012.
- [17] Z. Zhang, C. Shao, X. Li et al., "Electrospun nanofibers of ZnO-SnO₂ heterojunction with high photocatalytic activity," *The Journal of Physical Chemistry C*, vol. 114, no. 17, pp. 7920–7925, 2010.
- [18] S. Balachandran and M. Swaminathan, "Facile fabrication of heterostructured Bi₂O₃-ZnO photocatalyst and its enhanced photocatalytic activity," *The Journal of Physical Chemistry C*, vol. 116, no. 50, pp. 26306–26312, 2012.
- [19] S. Li, K. Yu, Y. Wang et al., "Cu₂S@ZnO hetero-nanostructures: facile synthesis, morphology-evolution and enhanced photocatalysis and field emission properties," *CrystEngComm*, vol. 15, no. 9, pp. 1753–1761, 2013.
- [20] F. Xu, Y. Yuan, H. Han, D. Wu, Z. Gao, and K. Jiang, "Synthesis of ZnO/CdS hierarchical heterostructure with enhanced photocatalytic efficiency under nature sunlight," *CrystEngComm*, vol. 14, no. 10, pp. 3615–3622, 2012.
- [21] S. Khanchandani, S. Kundu, A. Patra, and A. K. Ganguli, "Shell thickness dependent photocatalytic properties of ZnO/CdS core-shell nanorods," *The Journal of Physical Chemistry C*, vol. 116, no. 44, pp. 23653–23662, 2012.
- [22] T. B. Li, G. Chen, C. Zhou, Z. Y. Shen, R. C. Jin, and J. X. Sun, "New photocatalyst BiOCl/BiOI composites with highly enhanced visible light photocatalytic performances," *Dalton Transactions*, vol. 40, no. 25, pp. 6751–6758, 2011.

- [23] X. Zhang, Z. Ai, F. Jia, and L. Zhang, "Generalized one-pot synthesis, characterization, and photocatalytic activity of hierarchical BiOX (X = Cl, Br, I) nanoplate microspheres," *The Journal of Physical Chemistry C*, vol. 112, no. 3, pp. 747–753, 2008.
- [24] K. Zhang, D. Zhang, J. Liu et al., "A novel nanoreactor framework of iodine-incorporated BiOCl core-shell structure: enhanced light-harvesting system for photocatalysis," *CrystEngComm*, vol. 14, no. 2, pp. 700–707, 2012.
- [25] H. Cheng, B. Huang, X. Qin, X. Zhang, and Y. Dai, "A controlled anion exchange strategy to synthesize Bi₂S₃ nanocrystals/BiOCl hybrid architectures with efficient visible light photoactivity," *Chemical Communications*, vol. 48, no. 1, pp. 97–99, 2012.
- [26] S. Weng, B. Chen, L. Xie, Z. Zheng, and P. Liu, "Facile in situ synthesis of a Bi/BiOCl nanocomposite with high photocatalytic activity," *Journal of Materials Chemistry A*, vol. 1, no. 9, pp. 3068–3075, 2013.
- [27] J.-M. Song, C.-J. Mao, H.-L. Niu, Y.-H. Shen, and S.-Y. Zhang, "Hierarchical structured bismuth oxychlorides: Self-assembly from nanoplates to nanoflowers via a solvothermal route and their photocatalytic properties," *CrystEngComm*, vol. 12, no. 11, pp. 3875–3881, 2010.
- [28] L.-P. Zhu, G.-H. Liao, N.-C. Bing, L.-L. Wang, Y. Yang, and H.-Y. Xie, "Self-assembled 3D BiOCl architectures: tunable synthesis and characterization," *CrystEngComm*, vol. 12, no. 11, pp. 3791–3796, 2010.
- [29] M. Ge, Y. Li, L. Liu, Z. Zhou, and W. Chen, "Bi₂O₃-Bi₂WO₆ composite microspheres: hydrothermal synthesis and photocatalytic performances," *The Journal of Physical Chemistry C*, vol. 115, no. 13, pp. 5220–5225, 2011.
- [30] A.-J. Wang, Q.-C. Liao, J.-J. Feng, P.-P. Zhang, Z.-M. Zhang, and J.-R. Chen, "D-Penicillamine-assisted self-assembly of hierarchical PbS microstars with octa-symmetric-dendritic arms," *Crystal Growth & Design*, vol. 12, pp. 832–841, 2012.
- [31] Z. Wang, S.-W. Cao, S. C. J. Loo, and C. Xue, "Nanoparticle heterojunctions in ZnS-ZnO hybrid nanowires for visible-light-driven photocatalytic hydrogen generation," *CrystEngComm*, vol. 15, no. 28, pp. 5688–5693, 2013.
- [32] S. Zhang, Y. Du, H. Li et al., "Evidence of matrix lattice distortion in Zn_{1-x}Co_xO nanocrystals," *The Journal of Physical Chemistry C*, vol. 113, no. 11, pp. 4263–4269, 2009.



Hindawi

Submit your manuscripts at
<http://www.hindawi.com>

